Granular Matter (2025) 27:8
https://doi.org/10.1007/s10035-024-01487-3

RESEARCH

Effects of aggregate crushing and strain rate on fracture in compressive concrete with a DEM-based breakage model

Michal Nitka[1] · **Jacek Tejchman**[1]

Received: 23 August 2024 / Accepted: 12 November 2024

Abstract
This study looked at how breakable aggregates affected the mesoscopic dynamic behavior of concrete in the uniaxial compression condition. In-depth dynamic two-dimensional (2D) studies were conducted to examine the impact of aggregate crushing and strain rate on concrete's dynamic strength and fracture patterns. Using a DEM-based breakage model, concrete was simulated as a four-phase material consisting of aggregate, mortar, ITZs, and macropores. The concrete mesostructure was obtained from laboratory micro-CT tests. Collections of spherical particles were used to imitate aggregate breakage of different sizes and shapes by enabling intra-granular fracturing between them. The mortar was described in terms of unbreakable spheres with different diameters. Compared to the mortar, the aggregate strength was always stronger. A qualitative consistency was achieved between the DEM results and the available experimental data. Concrete's dynamic compressive strength rose significantly with strain rate and just somewhat with aggregate strength. The fracture process was impacted considerably by aggregate crushing and strain rate. The number of broken contacts grew with an increase in strain rate and a decrease in aggregate strength.

Keywords Concrete · Dynamic behavior · DEM · Uniaxial compression · Aggregate breakage

1 Introduction

The strain rate affects concrete. It is commonly reported that strain rate increases the tensile and compressive strength, elastic modulus, and peak strain (e.g [1–5]). The strengths increase more quickly at a threshold strain rate, roughly 50 1/s for compression and 1 1/s for tension. The failure mechanism also changes as the loading rate increases. The density of cracking increases with increasing strain rate. Two main processes are responsible for the rise in compressive strength: structural inertial forces [6, 7] and movement of viscous free water in micro-defects [8–11]. The first one generates radial inertial forces similar to lateral confining pressure. The second one generates fluid confinement in pores and cracks that slows the fracture process and increases strength. Furthermore, aggregate fragmentation is important for high strain rates [12–14]. The cracks propagate through coarse aggregate instead of moving along the weaker zones (mortar or interfacial transition zones (ITZs)) due to high-speed stress waves traveling fast through the specimen. Thus, the aggregate fragmentation process (typically more resilient than the mortar in standard concrete) might enhance concrete strength. There exist different types of aggregate particles for concrete in engineering practice (that make 60–80% of the volume of concrete) composed of e.g. basalt, granite, gabbro, amphibolite, dolomite, limestone, sandstone, etc. with a compressive strength ranging between 30 and 350 MPa.

The dry concrete behavior at the mesoscopic level under 2D dynamic uniaxial compression is the subject of the current numerical study. The goal of this study, which is new research, is to ascertain how strain rate and aggregate breakage into fine particles affect the dynamic concrete behavior at the mesoscopic scale compared to its quasi-static response. In our previous papers, the effect of viscous free water movement on the concrete response in compression and tension was investigated by ignoring the aggregate crushing [15, 16]. In the current paper, a 2D DEM-based breakage model was used wherein the impact of free water

✉ Jacek Tejchman
tejchmk@pg.edu.pl

[1] Faculty of Civil and Environmental Engineering, Gdansk University of Technology, Narutowicza 11/12, 80-233 Gdańsk, Poland

Published online: 26 November 2024

was neglected. A so-called clump breakage algorithm [17] was applied. Clumps composed of spheres were used to describe the aggregate particles of different diameters and shapes. The benefits of this method are that each initial clump of particles can be arranged to take a non-spherical shape and the fracture preserves mass. It provides a fair solution that approximates complex shapes well and maintains a simple contact detection algorithm. Concrete was assumed in simulations to be a four-phase material, including aggregate, mortar, ITZs adjacent to aggregates, and macro-pores [18–20]. The concrete mesostructure chosen in simulations was obtained from laboratory micro-CT tests (the aggregates with real shapes were imported into DEM).

The 2D model was used in the initial research stage to cut down on computation time. Through a series of 2D DEM simulations, the qualitative impacts of strain rate and aggregate strength were carefully examined for the same concrete specimen. The strain rate varied between 0.1/s and 1000 1/s. The aggregate strength was always stronger than the mortar (2, 5, or 10 times). The study focused on the strength and fracture pattern changes during dynamic concrete compression. The dynamic increase factor (DIF) was ascertained. A comparison was also made between the DEM results using breakable and unbreakable aggregates. Additionally, the damping coefficient's impact was looked into. The current 2D simulations were carried out for the future coupled 2D DEM-CFD computations [15, 16]. The 3D DEM/CFD model is ready, however, it requires huge computation time because it was parallelized on threads only. To shorten the computation time, it needs a distributed parallelization on cluster computer nodes, that is well underway. The 2D modeling does not provide quantitatively precise modeling of real 3D behavior; rather, it is an intermediary step toward understanding the physical model. The effects of inertia, fracture, fluid pressure, and velocities are quantitatively different in 3D than 2D conditions especially for very high strain rates, due to the various volume of pores/cracks and confining pressure. The 2D analyses instead of 3D ones have no qualitative impact on the nature of a purely mechanical problem [20].

The novel points of the paper are (a) the mesoscopic calculations of the effect of aggregate fragmentation on the compressive concrete-like materials' behavior under a wide range of strain rates, (b) the use of the real concrete mesostructure in mesoscopic dynamic computations, and (c) comparative calculations with breakable and unbreakable aggregate particles. Additionally, the impact of the damping coefficient on DEM outcomes was examined. The calculations were only for one concrete specimen (without material parametric studies). The DEM uniaxial compression outcomes were solely qualitatively compared with the experimental literature data from split Hopkinson pressure bar (SHPB) tests due to evident differences in both loading systems.

At present, SHPB has become a common laboratory tool to study the mechanical properties of materials under the high-speed impacts ($\dot{\epsilon}>10$ 1/s) like rock/ceramic/mortar/concrete (e.g [21–28]) by ensuring the dynamic force balance. Below this strain rate, a hydraulic servo testing system or drop-weight impactor may be used [29, 30]. In the SHPB test, the assumptions of one-dimensional stress waves and uniformity are crucial to the data analysis. The assumption of 1D stress wave propagation is ensured by very long metal bars (incident bar and transmitted bar) [22]. A relatively large specimen size for the bar diameters contributes to the material's uniformity [22]. The laboratory tests revealed that the increment of compressive strength of concrete was mainly caused by the confinement caused by the inertia effect [21–25]. As the strain rate increased, the peak stress and strain of concrete and elastic modulus gradually raised, confirming its strengthening effect. The rate dependence was stronger for high strain rates [24]. The dynamic compressive strength also raised with water saturation grade [31–33], static hydrostatic pressure [34], and wall friction [22]. The dynamic strength of concretes was higher than mortars due to the presence of aggregate particles [24] in contrast to quasi-static conditions. With an increasing strain rate, the softening rate rose [25] or was comparable [24]. The stress-strain curves were smooth even for very high strain rates [24, 25]. The dynamic compressive strengths of cylinders were higher than those of cubes [35]. For large strain rates, the impact of specimen sizes was determined to be negligible [35]. The higher the compressive strength, the lower the increase in the specimen strength under high loading rates [36, 37]. There was less result spread created by shorter specimens [37]. The dynamic response was a transient brittle failure process. The cracks propagated throughout the entire specimen including stronger aggregates. The degree of concrete fragmentation increased with the rise in the strain rate and the failure pattern progressed from cracking (but not fragmentation) for low strain rates to complete pulverization for very high strain rates [25, 35]. Regarding the strain rate ranges, the damage modes were divided into three categories: (a) numerous small cracks leading to failure, (b) major cracks or broken parts inside the specimens contributing to failure, and (c) total destruction of the specimens [35].

The literature created several mesoscopic discrete models for concrete mechanical behavior, including discrete element approaches, rigid-body-spring models, lattice discrete particle models, and classical lattice models [38]. We used DEM because it proved to be a realistic representation of a fracture process in concrete [18–20, 39–42], reinforced concrete [43], and rock [44]. Moreover, it more precisely

represents the material mesostructure and contact forces using simple dynamic equations. Grain fragmentation using DEM was extensively studied in the literature, mostly in the fields of mining and geotechnical engineering (e.g [45–57]). There are fewer DEM studies on the impact of aggregate breakage in concrete [17, 58]. In the paper [17], the effect of aggregate crushing on the propagation of a single crack in a notched beam during bending was investigated under various strain rates. The impact of the various strain rates was not considered during uniaxial compression in the paper [58]. However, those DEM results showed that coarse aggregate crushing had a noticeable influence on concrete deformation and failure characteristics.

The structure of the current paper is as follows. Section 2 provides a brief description of DEM following the introductory Sect. 1. The input data for the DEM simulations are explained in Sect. 3. Section 4 provides a detailed description of the findings from the dynamic numerical simulations regarding the impact of aggregate strength and strain rate on the behavior of concrete under uniaxial compression. A few conclusions are offered in Sect. 5.

2 DEM for cohesive-frictional materials

Numerical analyses were performed using YADE [59, 60], a 3D open-source DEM program that takes advantage of the so-called soft-particle approach (i.e. the DEM model allows for particle deformation that is simulated as an overlap of particles). Particles in DEM interact with one another during translational and rotational motions with the application of an explicit time-stepping technique and Newton's second law of motion [61]. An overlap between two contacted bodies is allowed. Due to the particle overlap, any microporosity may be reached. Because DEM takes into account inertial forces, it is a dynamic technique. The model predicts a cohesive bond at the grain contact with a brittle failure below the critical normal tensile force. Shear cohesion failure under typical compression results in contact stick and slip being governed by the Coulomb friction law. Regularization is not needed in DEM which does not use partial differential equations. Thus, DEM provides a well-posed discrete equation system. Figure 1 shows the mechanical response of DEM for particles. The following is a list of DEM formulas [59, 60]:

$$\vec{F}_n = K_n U \vec{N}, \tag{1}$$

$$\vec{F}_s = \vec{F}_{s,prev} + K_s \Delta \vec{X}_s, \tag{2}$$

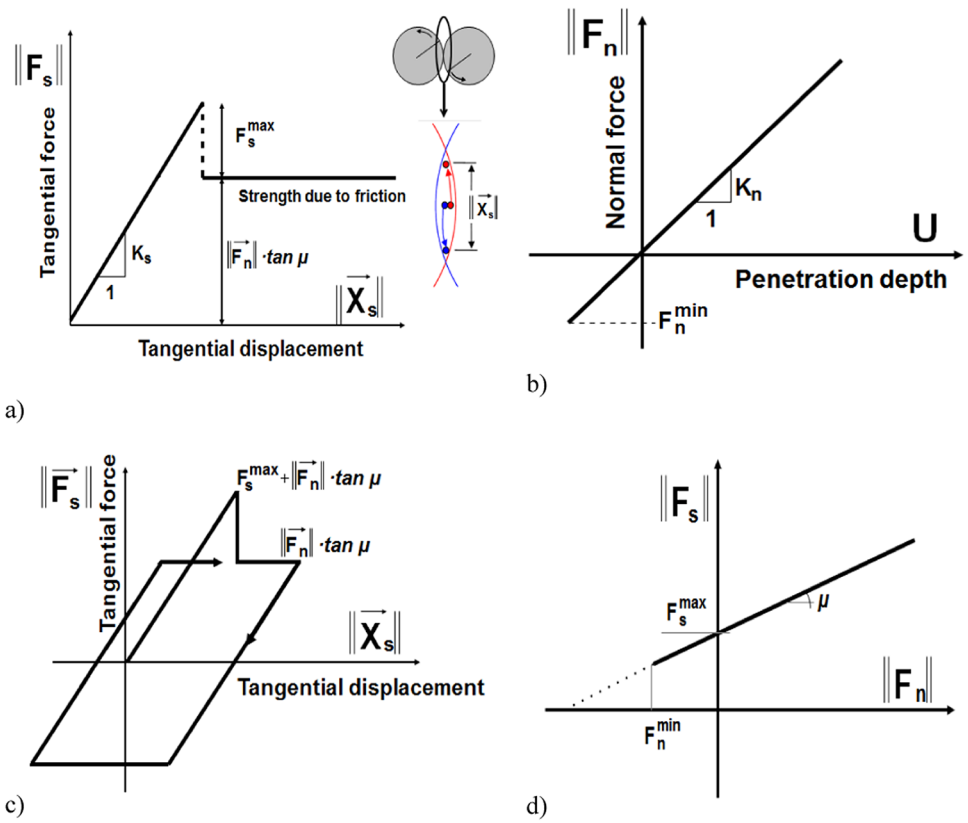

Fig. 1 Mechanical response of DEM: (**a**) tangential contact model, (**b**) normal contact model, (**c**) loading and unloading path in tangential contact model and (**d**) modified Mohr-Coulomb model [59, 60]

$$K_n = E_c \frac{2R_A R_B}{R_A + R_B} \quad \text{and} \quad K_s = v_c E_c \frac{2R_A R_B}{R_A + R_B}, \tag{3}$$

$$\left\|\vec{F}_s\right\| - F^s_{\max} - \left\|\vec{F}_n\right\| \times \tan\mu_c \leqslant 0 \quad \text{(before contact breakage)}, \tag{4}$$

$$\left\|\vec{F}_s\right\| - \left\|\vec{F}_n\right\| \times \tan\mu_c \leqslant 0 \quad \text{(after contact breakage)}, \tag{5}$$

$$F^s_{max} = CR^2 \quad \text{and} \quad F^n_{min} = TR^2, \tag{6}$$

$$\vec{F}^k_{damp} = \vec{F}^k - \alpha_d \cdot sgn\left(\vec{v}^k_p\right) \vec{F}^k \tag{7}$$

where $\vec{F}_n$ - the normal contact force, U - the overlap between discrete elements, $\vec{N}$ - the unit normal vector at the contact point, $\vec{F}_s$ - the tangential contact force, $\vec{F}_{s,prev}$ - the tangential contact force in the previous iteration, $\vec{X}_s$ - the relative tangential displacement increment, K_n - the normal contact stiffness, K_s - the tangential contact stiffness, E_c- the elastic modulus of the particle contact, v_c - the Poisson's ratio of particle contact, R - the particle radius, R_A and R_B contacting particle radii, μ_c - the Coulomb inter-particle friction angle, F^s_{max} - the critical cohesive contact force, F^n_{min} - the minimum tensile force, C - the cohesion at the contact (maximum shear stress at zero pressure), and T - the tensile strength of the contact, $\vec{F}^k_{damp}$ - the dampened contact force, $\vec{F}^k$ and $\vec{v}^k_p$ - k^{th} components of the residual force and translational particle velocity v_p and α_d - the positive damping coefficient smaller than 1 (sgn(•) that returns the sign of the k^{th} component of velocity).

The following material constants are required for DEM simulations: E_c, v_c, μ_c, C, and T. Non-viscous damping was assumed [62] (Eq. 7) in simulations. Additionally necessary are the parameters R, ρ (mass density), and α_d. To accurately replicate the distribution of shear and tensile cracks, the relationship between the uniaxial compressive and tensile strength, and the failure mode of specimens (brittle or quasi-brittle, shear or tensile), the particle contact ratio C/T must be carefully considered [44]. As the C/T ratio grows, a more brittle and tensile failure mode dominates, and more tensile cracks appear. Typically, the material constants in DEM are determined by running several simulations and comparing the outcomes to experimental data from simple tests, such as uniaxial compression, triaxial compression, and simple shear.

If a cohesive joint (Eq. 6) between two elements vanished after crossing a critical threshold, damage was presumed. If any contacts between spheres were restored following failure, there was no cohesion (Eq. 6). The DEM model did not account for material softening. The model was successfully used by the authors to represent the behavior of numerous engineering materials having a particulate structure, such as granulates [63–66], concrete [18–20, 39–42], reinforced concrete [43], and rocks [44, 67, 68]. Due to calculating time constraints, DEM cannot be recommended as a numerical tool for large concrete or reinforced concrete elements. There exist some up-scaling techniques used in DEM, such as mass/density/gravity scaling or grain up-scaling (precise scaling of grains and coarse-graining). However, when strain localization occurs in concrete, those up-scaling techniques fail since the size of the localized zone cannot be scaled (because it depends on the initial and boundary conditions of the entire system).

3 Input data for DEM simulations

A square concrete specimen 50×50 mm^2 geometry was assumed in 2D analyses. The depth of the specimen was equal to the grains' diameter. The bottom boundary was vertically fixed. Vertical boundaries were free and horizontal boundaries were smooth to eliminate a size effect due to wall friction. The dynamic compressive strength rises with increasing wall friction and decreasing specimen size [22, 69]. A constant vertical velocity v was applied along the upper horizontal boundary to deform the specimen (as during a standard uniaxial compression test). A single vertical displacement increment was equal to 5^{-10} m (based on preliminary simulations).

Concrete was modeled as a four-phase material composed of mortar, aggregate, ITZs, and macro-pores. The porous ITZs surrounding aggregate particles were characterized as weaker contacts that lacked a defined physical width [18–20]. The macropores in the mortar (only with a diameter ≥ 1 mm) were modeled as empty regions of circular shape [18, 20]. The effect of macropores on the shape of macro-cracks is not as important as that of ITZs since it rarely happens that the macro-cracks propagate through macropores [18]. The aggregate's range in concrete was $d = 1$–16 mm. Based on micro-CT images, the mesostructure was presumed to be from the actual concrete specimen [18, 70]. The aggregate's range on the micro-CT image $d = 1$–8 mm. The clusters of 0.25–0.50 mm diameter spheres were always used to create the aggregate particles (independently of their size) for faithfully reproducing their real shapes. The spheres with diameters of 0.25–0.50 mm were also used to simulate the mortar particles. The effect of d_{min} in the mortar on the stress-strain curve in quasi-static DEM simulations was negligible if d_{min} was small enough, i.e. $d_{min} \leq 0.25$–0.50 mm [40]. The specimen's initial porosity was $p = 5\%$ [18, 70]. The material disorder existed in the specimen since the forces $F_{max}{}^s$ and $F_{min}{}^n$ depended on the particle radius to the power 2 (Eq. 6). The shrinkage and the subsequent pre-damage were neglected.

In DEM simulations, we assumed the material constants in the mortar similar to the previous analyses of concrete fracture [18–20, 39–42]. They are listed in Table 1 (with the C/T ratio equal to 2 [44]). In the case of ITZs, the ratio $E_{c,\ ITZ}/E_{c,\ cm}$=0.70 was chosen [18–20, 39–42], based on the nanoindentation experiments [71]. The remaining two ratios in ITZs, C_{ITZ}/C_{cm} and T_{ITZ}/T_{cm}, were also assumed to be equal to 0.70 due to a lack of experimental data for mortars of different initial porosity. Other calculations showed a significant impact of ITZ properties on the strength, brittleness, and fracture process of concrete [18]. Based on triaxial compression tests with clumped granulates, the inter-particle friction angle of $\mu_c = 18^o$ was postulated [72]. The damping factor was mainly set to $\alpha_d = 0.05$ (approximately equal to the material damping of concrete [73]). The time step was chosen as $\Delta t = 1 \times 10^{-8}/\dot{\epsilon}$. A total of 30,000 spherical elements were used, with 18,000 elements modeling mortar and 12,000 elements modeling aggregate. The initial coordination number was 4.6. About 1–2 days were needed to perform the DEM calculations on a computer with a 3.30 GHz CPU (1 day for the low strain rate and 2 days for the very high strain rate).

The DEM calculations were also carried out with the unbreakable aggregate. To avoid aggregate cracking, the material parameters were prescribed to the mortar and ITZs only, but not to the aggregate particles composed of clusters of spheres connected as rigid bodies [20–22]. Thus, the aggregate particles were also non-deformable. As the contact elasticity and strength of the aggregate increased, the number of aggregate cracks diminished (Fig. 12 in Sect. 4).

Table 1 Main DEM parameters for different phases in concrete assumed in dynamic simulations

Material parameters	Aggregate	Mortar	ITZs around aggregates
T [MPa]	48 (200% of mortar), 120 (500% of mortar), 240 (1000% of mortar), non-deformable	24	16.8 (70% of mortar)
C [MPa]	96 (200% of mortar), 240 (500% of mortar), 480 (1000% of mortar), non-deformable	48	33.6 (70% of mortar)
E_c [GPa]	22.4 (200% of mortar), 56 (500% of mortar), 112 (1000% of mortar), non-deformable	11.2	7.8 (70% of mortar)
υ_c [-]	0.2	0.2	0.2
μ_c [°]	18	18	18

4 DEM simulation results

Figures 2, 3, 4, 5, 6, 8 and 10, 11, 12 and 13 demonstrate the 2D DEM results with breakable aggregate for a dry concrete specimen with varying strain rates (0.1/s $\leq\dot{\epsilon}\leq$ 1000 1/s) and aggregate properties of Table 1. The dynamic stress-strain curves are shown in Fig. 2 ($\sigma = f(\varepsilon_y)$, where σ - vertical normal stress and ε_y - vertical normal strain). Figure 2a, c, and d includes the stress-strain curves for $\dot{\epsilon} \leq$ 100 1/s, and Fig. 2b for $\dot{\epsilon} \leq$ 1000 1/s. The static/dynamic compressive strength was calculated as the mean maximum vertical normal force calculated along the top and the bottom divided by the specimen area (width times depth). The vertical normal strain was calculated as the displacement increment related to the initial specimen height (engineering strain). A relationship between the compressive strength of concrete f_c and aggregate strength for different strain rates is shown in Fig. 3. Figures 4, 5 and 6 present the fracture patterns (based on displacements) in the deformed specimens at the failure and at the stress peak (the displacements were magnified by a factor of 2). The maps of broken contacts (equivalent to cracks) in three concrete phases (mortar, ITZs, and aggregate) for four different strain rates are demonstrated in Fig. 8. The evolution of the relative damaged contact number N [%] in three concrete phases versus the specimen strain is depicted in Figs. 10, 11, 12 and 13. For comparison, the stress-strain curves (Fig. 2d), fracture patterns (Fig. 7), maps of broken contacts (Fig. 9), and the evolutions of the relative damaged contact number (Fig. 14) are also provided for the concrete specimen with unbreakable and non-deformable aggregate particles.

4.1 Stress-strain curves

The concrete compressive strength, elastic modulus, vertical strain corresponding to the strength, and post-peak toughness strongly raised with increasing strain rate as in the experiments (e.g. [13, 22, 24, 32, 34] (Fig. 2). The material softening rate slightly raised for $\dot{\epsilon}$<0.10 1/s and later for $\dot{\epsilon}\geq$0.10 1/s remained similar independently of the aggregate strength in agreement with the experiments [22, 24, 32], but in discord with the experiments [13] (where it was rising for high strain rates). With a vertical normal strain of between $\varepsilon_y = 0.18\%$ and $\varepsilon_y = 0.28\%$, the predicted dynamic compressive strength was $f_c \cong$44-47 MPa and the global elastic modulus was E = 20–30 GPa for the strain rate $\dot{\epsilon}$=0.1 1/s (Fig. 2). For $\dot{\epsilon}$=100 1/s, the predicted dynamic compressive strength was estimated as f_c=130–150 MPa with a vertical normal strain of roughly $\varepsilon_y = 1\%$ and the elastic modulus was E = 50–100 GPa (Fig. 2). The mean compressive strength's growth (based on DEM simulations with three different aggregate strengths) was, thus, about 3. The

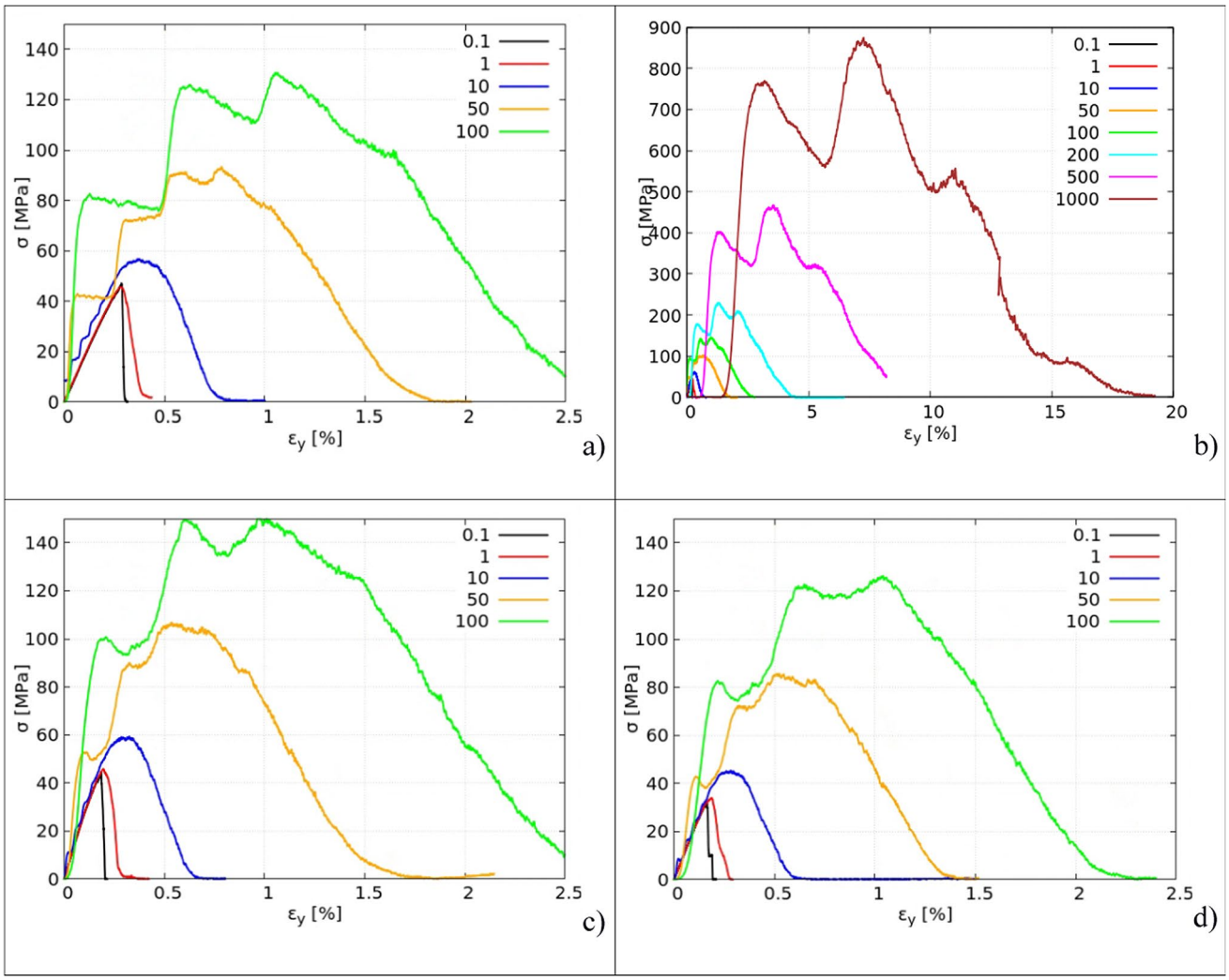

Fig. 2 DEM results: relationship between vertical normal stress σ and vertical normal strain ε_y for different strain rates (0.1/s $\leq\dot{\epsilon}\leq$ 1000 1/s) with various breakable aggregate properties (Table 1): (**a**) mortar parameters multiplied by factor 2, (**b**) mortar parameters multiplied by factor 5, (**c**) mortar parameters multiplied by factor 10 and (**d**) non-breakable aggregate

stress oscillations in the pre-peak regime due to the wave dispersion and reflection raised with increasing strain rate in contrast to SHPB tests where they were negligible. For $\dot{\epsilon}$ =1000 1/s, the mean strength's growth was already about 18 (Fig. 2b), i.e. too high as compared with SHPB experiments. The vertical normal strain corresponding to the strength was also too high. The differences between the dynamic vertical forces calculated along the specimen top and bottom at the peak stress were $\dot{\epsilon}\leq$3% ($\dot{\epsilon}\leq$10 1/s) and $\dot{\epsilon}\leq$11% ($\dot{\epsilon}\leq$1000 1/s). The sound speed in concrete, based on the elastic modulus E and density of concrete ρ was about 3000 m/s ($\dot{\epsilon}$=1 1/s) and 5000 m/s ($\dot{\epsilon}$=100 1/s), i.e. significantly higher than the sound velocity in the air (340 m/s).

The effect of the aggregate strength on the concrete strength was slight; it raised with the increase in the strength of the breakable aggregate. This increase was negligible (0.5%) in quasi-static simulations and 15% in dynamic analyses with $\dot{\epsilon}$=100 1/s (strong aggregate) (Fig. 2). As the strain rate rose, the dynamic stress oscillation became more noticeable. The average normal contact force at the peak stress was 0.94 N ($\dot{\epsilon}$=1 1/s), 1.23 N ($\dot{\epsilon}$=10 1/s), 3.21 N ($\dot{\epsilon}$=100 1/s), and 19.5 N ($\dot{\epsilon}$=1000 1/s). Since cracks were only produced in the mortar, which was weaker than the aggregate, the unbreakable and non-deformable aggregate particles (Fig. 2d) produced the lowest concrete strength, which was on average 20–30% less than that of the breakable aggregate.

4.2 Fracture

The crack patterns in the concrete specimen were composed mainly of variously inclined cracks (Figs. 4 and 5). The cracks occurred in the entire specimen. Their number increased with the growing strain rate. For $\dot{\epsilon}\leq$10 1/s, they

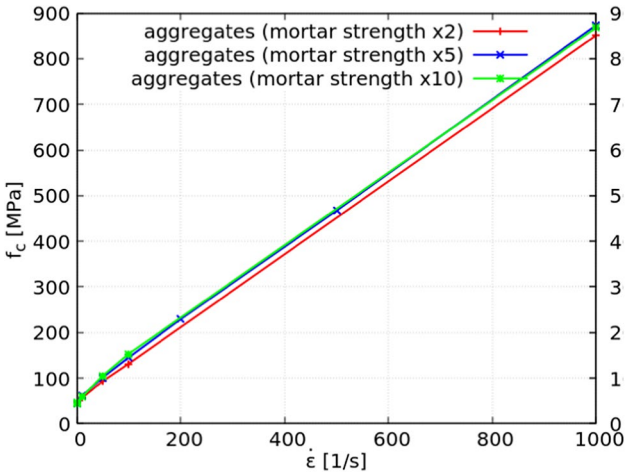

Fig. 3 DEM results with aggregate breakage: relationship between compressive strength f_c and aggregate strength for different strain rates $\dot{\epsilon}$ =0.1-1000 1/s (**a**) mortar parameters multiplied by factor 2, **b**) mortar parameters multiplied by factor 5, **c**) mortar parameters multiplied by factor 10)

were successively created in the weak ITZs (ε_y=0.1%), mortar (ε_y=0.15%), and breakable aggregate (ε_y=0.25–0.5%) (Figs. 10, 11, 12 and 13). For $\dot{\epsilon}$=100 1/s and $\dot{\epsilon}\leq$1000 1/s, the cracks started to co-occur in ITZs, mortar and aggregate. For very high strain rates ($\dot{\epsilon}$=1000 1/s), the specimens were almost totally fractured (Figs. 4 and 5, and 8) as in the experiments [25, 33]. The fracture patterns were similar for the strain rates $\dot{\epsilon}$=0.1 1/s and $\dot{\epsilon}$=1 1/s (Fig. 4). At the stress peak, several cracks were already created for $\dot{\epsilon}\geq$10 1/s only (Fig. 6). However, many cracks already occurred at this moment for $\dot{\epsilon}$=1000 1/s. Cracks in the aggregate appeared even in a quasi-static regime when the aggregate was twice as strong as the mortar (Figs. 4a and 8a with $\dot{\epsilon}$=0.1 1/s). Such a phenomenon also occurs in quasi-static laboratory experiments with the usual aggregate [19, 39, 40]. For the aggregate ten times stronger than the mortar, macro-cracks started to form in the aggregate from $\dot{\epsilon}$=50 1/s (Figs. 5c and 12c). When the huge contact elasticity and strength of aggregate particles were assumed, the aggregate cracks vanished for all strain rates. With an increasing strain rate, the damage rate (expressed by the number of broken contacts) non-linearly increased (approximately parabolically) (Figs. 10, 11, 12 and 13). The initial number of contacts was 47 622 (mortar), 4 838 (ITZs), and 31 776 (aggregate). As the strain rate increased and the aggregate strength decreased, there was a significant rise in the number of broken contacts in the mortar, ITZs, and aggregate (Figs. 10, 11 and 12). For the range $\dot{\epsilon}\leq$100 1/s, the damage rate was the greatest in ITZs, next in the mortar, and finally in the aggregate. The final relative number of broken contacts in the mortar raised from 20% ($\dot{\epsilon}$=0.1 1/s) to 60% ($\dot{\epsilon}$=100 1/s), in ITZs from 40 to 50% ($\dot{\epsilon}$=0.1 1/s) to 75–85% ($\dot{\epsilon}$=100 1/s), and in the aggregate from 0 to 10% ($\dot{\epsilon}$=0.1 1/s) to 15–50% ($\dot{\epsilon}$=100 1/s) (Figs. 10, 11 and 12). For $\dot{\epsilon}$=1000 1/s, the damage rate was the greatest in both ITZs and mortar and slightly less in the aggregate (Fig. 13). The final relative number of broken contacts in the mortar increased to 80% in the mortar and ITZs, and to 70–80% in the aggregate (Fig. 13) confirming the almost total specimen fracturing. In summary, the experimental damage modes were similar to those in the experiments [35]. Only the mortar and ITZs developed cracks when unbreakable and non-deformable aggregate particles were chosen. Figure 9 shows a significant difference in fracture patterns compared to Fig. 8 since the cracks could not propagate through aggregate particles. The fraction of broken contacts in the mortar and ITZs (Fig. 14) was marginally different from that of the breakable and non-deformable aggregate (Figs. 10, 11 and 13).

The aggregate size distribution curves (1–8 mm) caused by aggregate fragmentation for various strain rates $\dot{\epsilon}$ ranging from 0.1 1/s to 100 1/s with the mortar parameters multiplied by factor 2 is demonstrated in Fig. 15 (for $\dot{\epsilon}$=1000 1/s, the specimens were destroyed). The aggregate fragmentation caused the growth of the smaller aggregate particles as indicated by the lift of the curves N=f(D) with a rising strain rate. The aggregate size distribution curves after fragmentation showed small changes in shape due to several cracks running through shorter aggregate sizes (thus, the broken particles had the same diameter as the original particle).

Usually, the higher the damping coefficient, the higher the strength is obtained [39, 74]. The DEM calculation results (not shown here) demonstrated that the assumption of lower damping coefficients than α_d=0.05 (Eq. 6) insignificantly affected the results in Fig. 2.

4.3 Dynamic increase factor (DIF)

The dynamic increase factor (DIF) is the ratio of dynamic strength to quasi-static strength. This is widely used to explain how strain rate affects cement-based materials' dynamic mechanical properties [20–28]. Usually, a logarithmic scale of $\dot{\epsilon}$ is used to illustrate it.

In Fig. 16, the numerical and experimental values of DIF are shown for uniaxial compression on a logarithmic scale (between −1 and 3) against the strain rate. The calculated curve DIF = f(log($\dot{\epsilon}$)) from DEM analyses resembled the one assumed in CEB-FIP [75], based on laboratory test results. DIF non-linearly increased with the growing strain rate in DEM analyses. The increase started to be pronounced for $\dot{\epsilon}$ >10 1/s. The DIF values in the DEM simulations were equal to 1.05 ($\dot{\epsilon}$=1 1/s), 1.15 ($\dot{\epsilon}$=10 1/s), 1.80 ($\dot{\epsilon}$=50 1/s), 2.40 ($\dot{\epsilon}$=100 1/s), and 18 ($\dot{\epsilon}$=1000 1/s) (Fig. 16). The experimental DIF values in [75] were slightly lower than the numerical

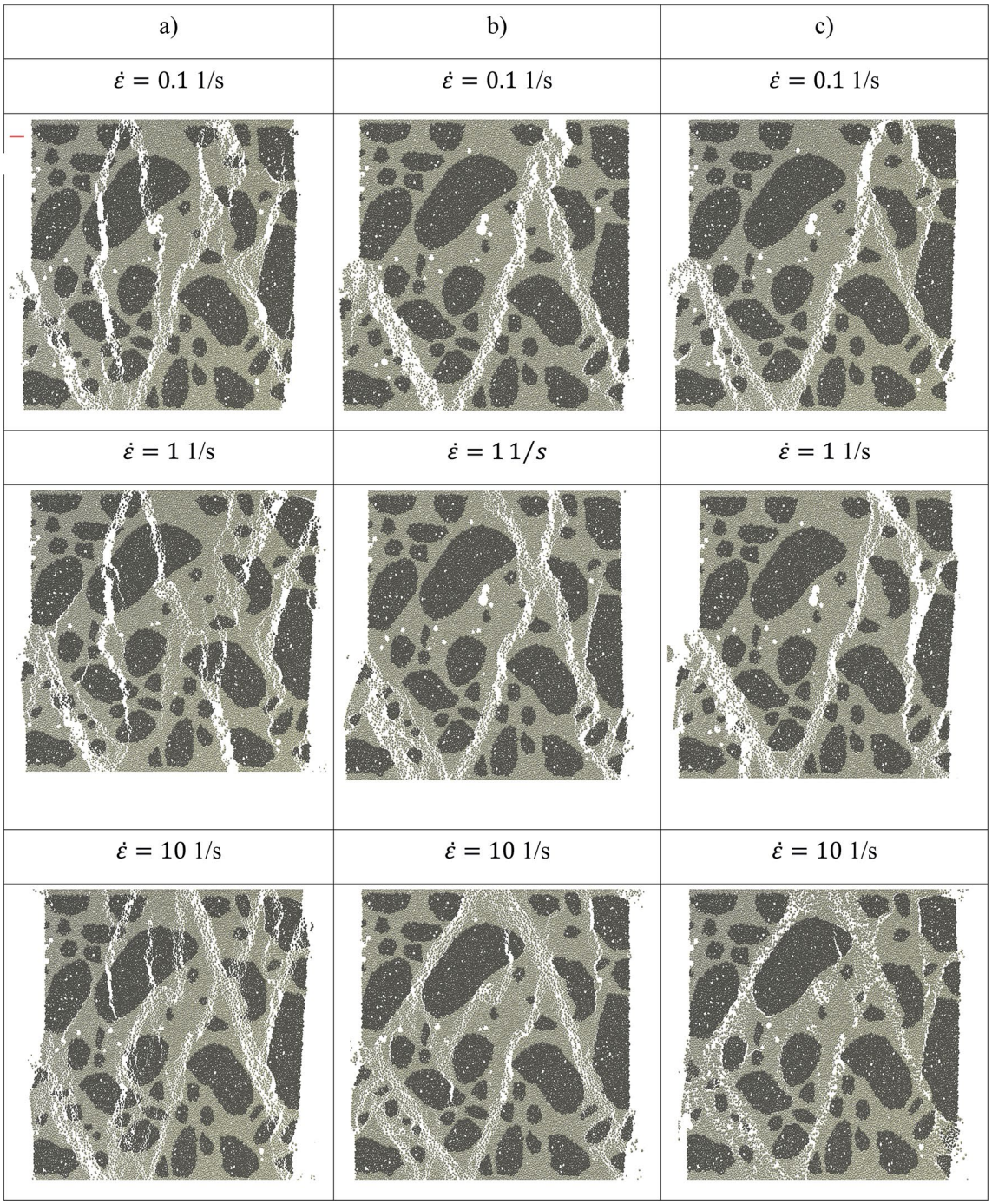

Fig. 4 DEM displacement results with aggregate breakage: evolution of fracture at failure for different strain rates (0.1 1/s≤ $\dot{\epsilon}$ ≤10 1/s) with various aggregate parameters (Table 1): (**a**) mortar parameters multiplied by factor 2, (**b**) factor 5 and (**c**) factor 10 (displacements are magnified by factor 2, macropores are marked as white spots)

ones for $\dot{\epsilon}$ ≤100 1/s: 1.05 ($\dot{\epsilon}$=1 1/s), 1.10 ($\dot{\epsilon}$=10 1/s), 1.40 ($\dot{\epsilon}$=50 1/s) and 1.80 ($\dot{\epsilon}$=100 1/s). However, they were significantly too low for the higher strain rates $\dot{\epsilon}$>100 1/s (e.g. DIF=6.2<<18 for $\dot{\epsilon}$=1000 1/s) (Fig. 16).

Different loading systems considered in dynamic experiments (compressive SHPB tests) and DEM dynamic analyses (standard uniaxial compression) are the primary causes of the DIF disparities mentioned above. The specimen deformation in SHPB testing, where 1D stress wave propagation is guaranteed by long metal bars, is significantly more uniform than in 2D DEM simulations, especially at high strain rates, which contributes to the variations in DIF results. Different concrete mesostructures and specimen geometries and shapes are further factors influencing the

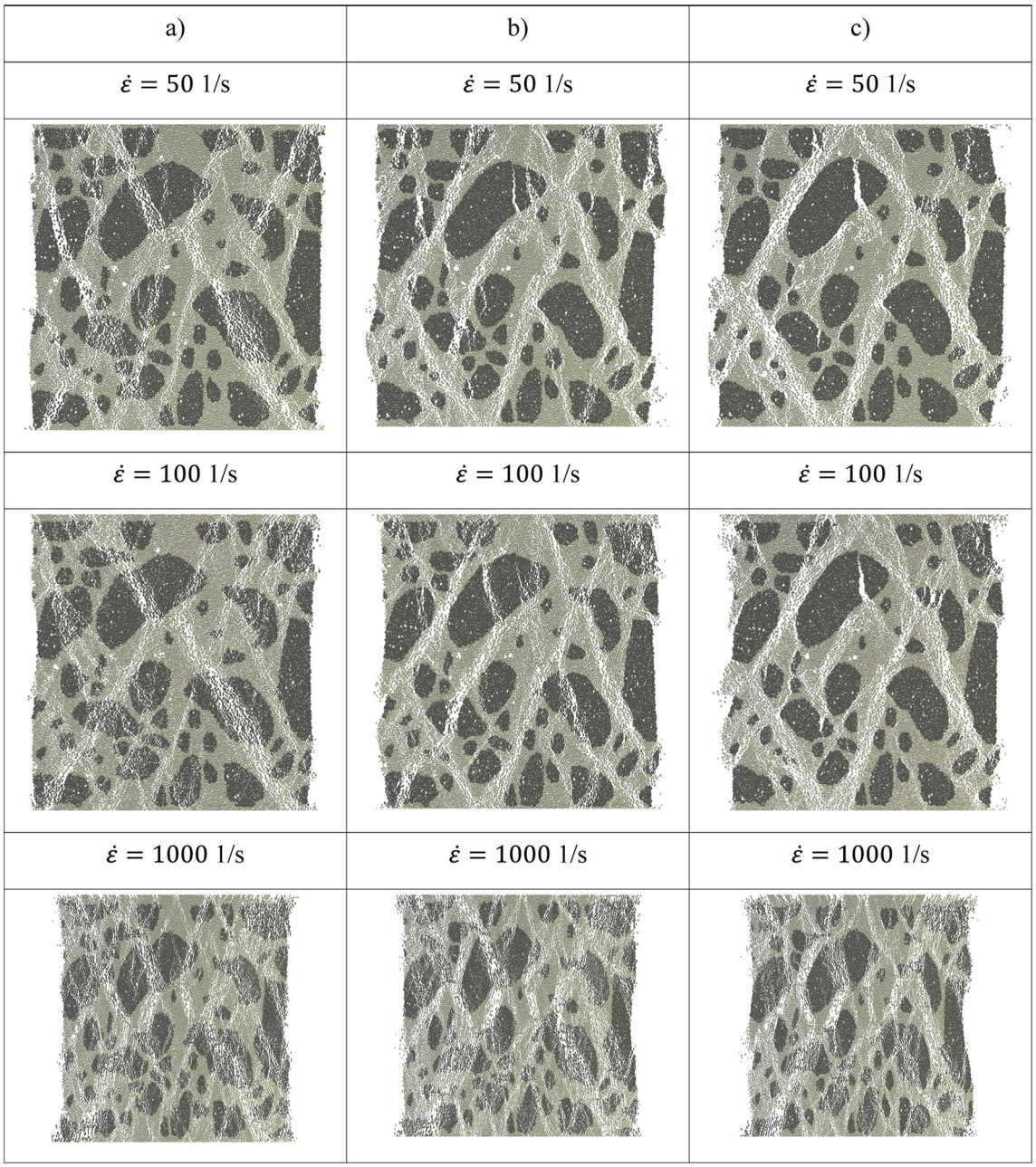

Fig. 5 DEM displacement results with aggregate breakage: evolution of fracture at failure for different strain rates (50 1/s≤ $\dot{\epsilon}$ ≤1000 1/s) with various aggregate parameters (Table 1): (**a**) mortar parameters multiplied by factor 2, (**b**) factor 5 and (**c**) factor 10 (displacements are magnified by factor 2, macropores are marked as white spots)

discrepancies between the experimental and numerical DIF results (in SHPB tests, cylindrical specimens with a slenderness ratio of 0.5-1.0 are usually employed). The numerical DIF value may also be affected by the quantity of fine particles that make up the aggregate, the material parameters (such as the *C/T* ratio and ITZ properties in relation to the mortar, Table 1), and mortar porosity. Furthermore, the existing calculations did not account for the migration of viscous free water in the pores and cracks of concrete specimens, which affects the behavior of concrete [15, 16]. More cracks are formed at high aggregate fragmentation, which could reduce the amount of free water confinement in pores and cracks and weaken the concrete. This will lead to a reduced computed DIF during standard uniaxial compression (Fig. 16). In the following research step, coupled dynamic 2D DEM-CFD calculations for both uniaxial and SHPB compression within a broad strain rate range will take into account the combined impacts of strain rate, aggregate breakage, and free water flow [76].

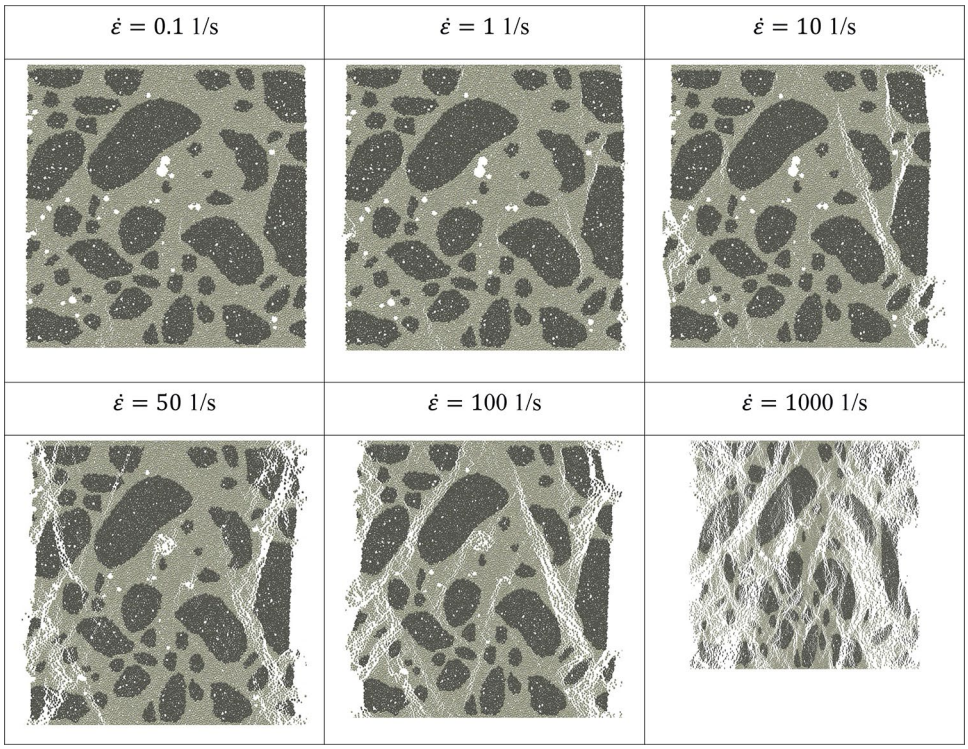

Fig. 6 DEM displacement results with aggregate breakage: evolution of fracture at stress peak for different strain rates ($0.1/s \leq \dot{\epsilon} \leq 1000$ 1/s) with mortar parameters multiplied by factor 10 in aggregate (displacements are magnified by factor 2, macropores are marked as white spots)

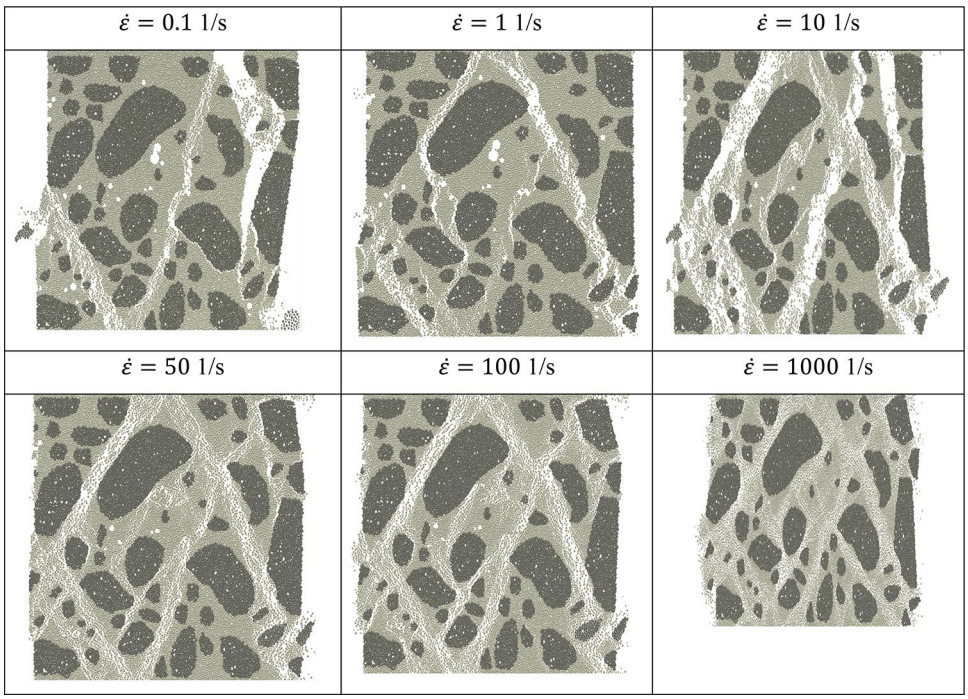

Fig. 7 DEM displacement results with unbreakable and non-deformable aggregate: evolution of fracture at failure for different strain rates (0.1 1/s$\leq \dot{\epsilon} \leq 1000$ 1/s) (displacements are magnified by factor 2, macropores are marked as white spots)

5 Summary and conclusions

This computational study examined how concrete behaved under dynamic uniaxial compression in simplified 2D dynamic settings regarding a stress-strain curve and fracture process. A DEM-based breakage model was established for concrete that was simulated using a four-phase material including aggregate, mortar, ITZs, and macro-pores. The width of ITZs was equal to zero. The ITZ stiffness and strength were 30% weaker than in the mortar. The DEM simulations assumed different strain rates between 0.1 1/s and 1000 1/s and three different aggregate strengths which were always higher than the mortar ones (two, five, or ten times). The impact of the strain rate and aggregate strength

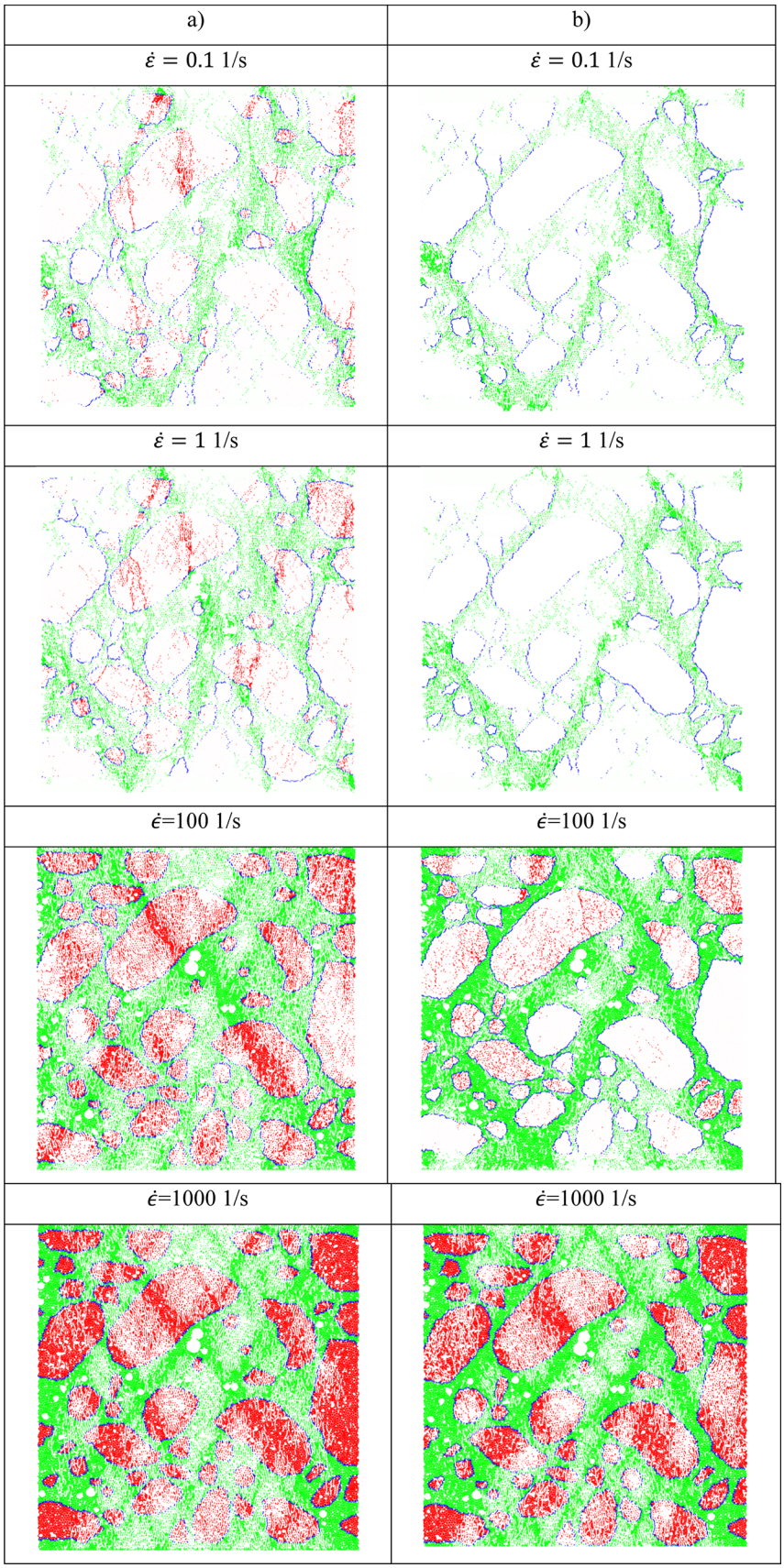

Fig. 8 DEM results with aggregate breakage: fracture patterns in non-deformed specimens for different strain rates (0.1 1/s≤ $\dot{\epsilon}$ ≤1000 1/s) with two various aggregate parameters (Table 1): (**a**) mortar parameters multiplied by factor 2 and (**b**) factor 10 (red color – broken aggregate, blue color – broken ITZs and green color – broken mortar)

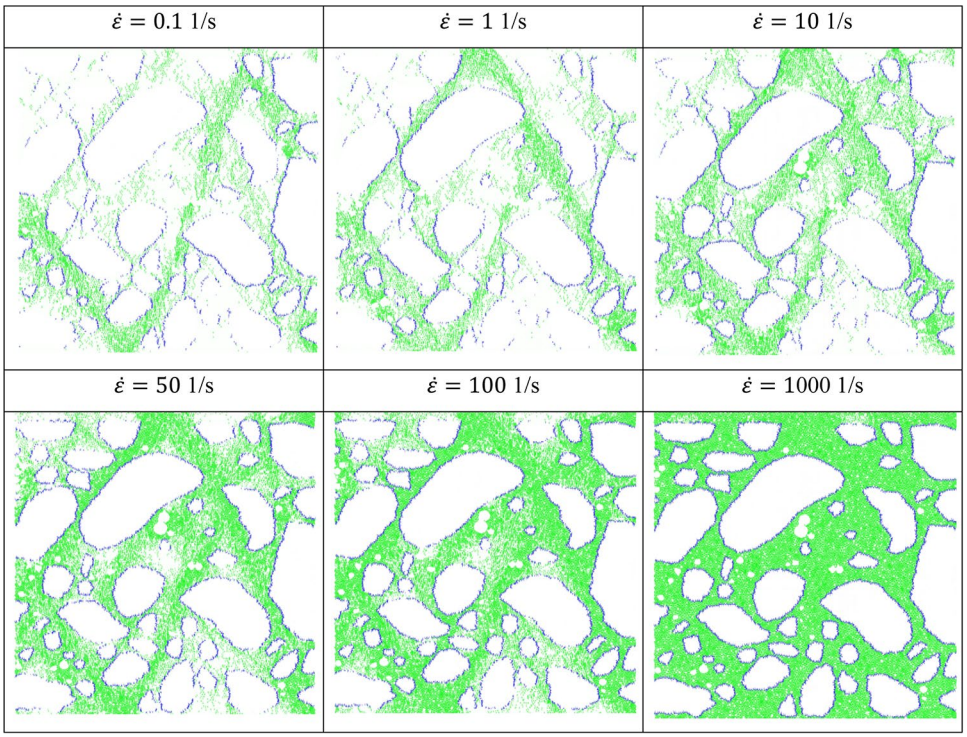

Fig. 9 DEM results with unbreakable and non-deformable aggregate particles: fracture patterns in undeformed specimens for different strain rates (0.1 1/s≤ $\dot{\epsilon}$ ≤1000 1/s (blue color – broken ITZs and green color – broken mortar)

on a fracture process proved to be noticeable. The following findings of the 2D mesoscopic dynamic simulations of concrete specimens under standard uniaxial compression can be offered:

- The strain rate significantly impacted the concrete's mechanical response following the existing literature research outcomes. The concrete compressive strength, elastic modulus, peak strain corresponding to the strength, and post-peak toughness strongly increased with increasing strain rate, exhibiting a notable strain rate strengthening effect as in experiments. The material softening rate initially rose with the strain rate (up to $\dot{\epsilon}$ =10 1/s) and later remained similar.
- The concrete strength dropped with the fall of the strength of the breakable aggregate in the considered strength range. The drop was only 0.5% in quasi-static calculations and increased in dynamic calculations, up to 15% with $\dot{\epsilon}$=1000 1/s. The concrete strength for the unbreakable and non-deformable aggregate was lower on average by 20–30% than for the breakable aggregate.
- The patterns of cracks consisted of many inclined cracks. The cracks propagated throughout the entire specimen including aggregate particles. For low strain rates, the fracture process varied between cracks (but not fragmentation), and for huge strain rates ($\dot{\epsilon}$=1000 1/s), it underwent complete pulverization. As the strain rate increased, the specimen cracking grew. The damage rate, based on the evolution of broken contacts, non-linearly increased (approximately parabolically). The ITZs, mortar, and breakable aggregate all developed cracks one after the other for $\dot{\epsilon}$≤10 1/s. For huge strain rates, they started to co-occur from the beginning of deformation. Even in the quasi-static tests, cracks were seen in the breakable aggregate. The crack patterns on concrete with unbreakable and non-deformable aggregate particles strongly differed from those for breakable ones.
- For the strain rate $\dot{\epsilon}$≤100 1/s, the damage rate was the greatest in ITZs, next in the mortar, and finally in the aggregate. The final relative number of broken contacts in the mortar raised from 20% ($\dot{\epsilon}$=0.1 1/s) to 60% ($\dot{\epsilon}$=100 1/s), in ITZs from 40 to 50% ($\dot{\epsilon}$=0.1 1/s) to 75–85% ($\dot{\epsilon}$ =100 1/s), and in the aggregate from 0 to 10% ($\dot{\epsilon}$=0.1 1/s) to 15–50% ($\dot{\epsilon}$=100 1/s). For =1000 1/s, the damage rate was the greatest in both ITZs and mortar and slightly less in the aggregate. The final relative number of broken contacts in the mortar increased to 80% in the mortar and ITZs, and to 70–80% in the aggregate. It was also higher in ITZs than in the mortar in concrete specimens including unbreakable and non-deformable aggregate particles. The differences in the number of broken contacts in the mortar and ITZs between breakable and unbreakable aggregate particles were marginal.
- The dynamic compressive SHPB laboratory tests and the DEM results (fracture patterns, stress-strain curves, and failure modes) agreed qualitatively. The calculated strength and corresponding strain, however, were excessively high. Furthermore, in DEM simulations, pre-peak

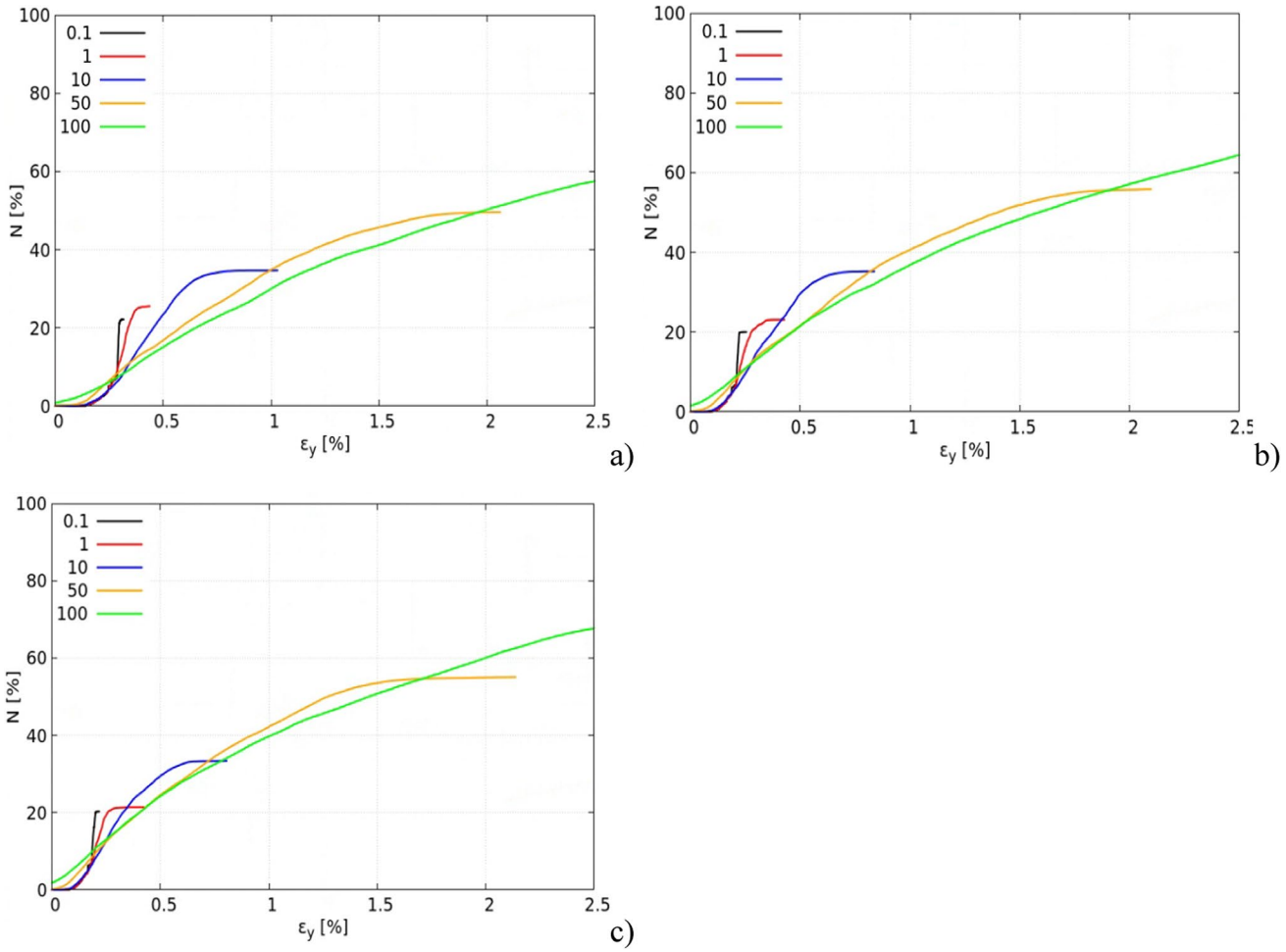

Fig. 10 DEM results with aggregate breakage: relative number of broken contacts at failure in ITZs for different strain rates (0.1 1/s≤ $\dot{\epsilon}$ ≤100 1/s) with various aggregate parameters: (**a**) mortar parameters multiplied by factor 2, (**b**) mortar parameters multiplied by factor 5 and (**c**) mortar parameters multiplied by factor 10

stress oscillations were observed. For the strain rate ≤100 1/s, the numerical DIF values were marginally greater than the experimental CEB-FIP values from compressive SHPB tests. The higher deformation non-uniformity in a standard dynamic uniaxial compression, which resulted from a different loading system than in a dynamic compressive SHPB test, caused them to be noticeably too high for >100 1/s.

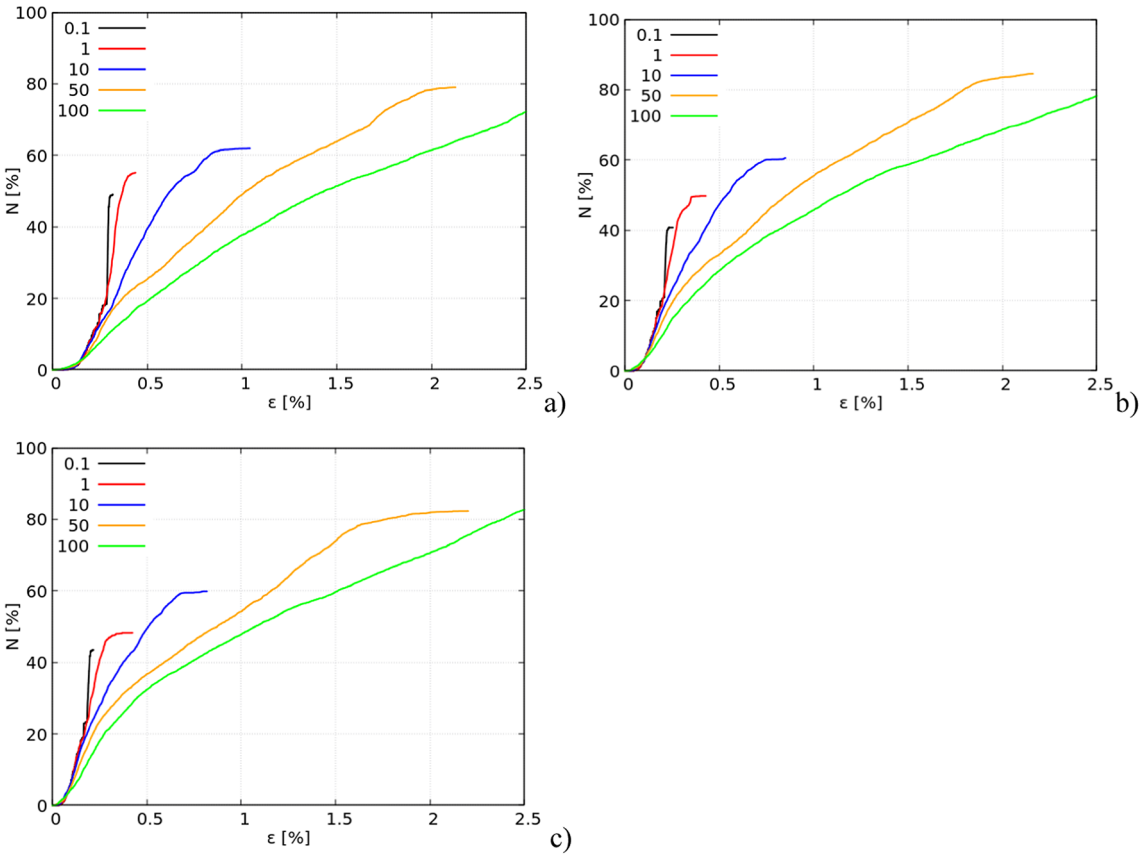

Fig. 11 DEM results with aggregate breakage: relative number of broken contacts at failure in mortar versus vertical normal strain ε_y for different strain rates (0.1 1/s≤ $\dot{\epsilon}$ ≤100 1/s) with various aggregate parameters: (**a**) mortar parameters multiplied by factor 2, (**b**) mortar parameters multiplied by factor 5 and (**c**) mortar parameters multiplied by factor 10

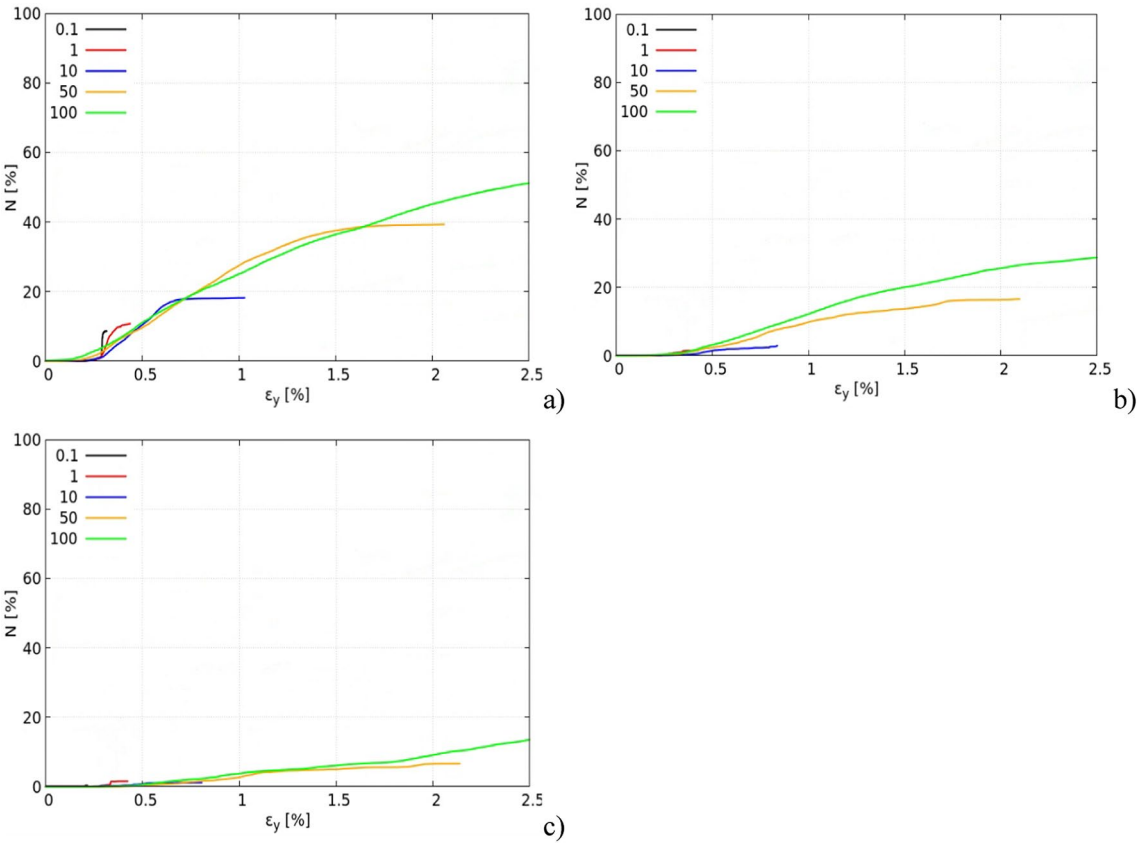

Fig. 12 DEM results with aggregate breakage: relative number of broken contacts at failure in aggregate for different strain rates (0.1 1/s≤ $\dot{\epsilon}$ ≤100 1/s) with various aggregate parameters: (**a**) mortar parameters multiplied by factor 2, (**b**) mortar parameters multiplied by factor 5 and (**c**) mortar parameters multiplied by factor 10

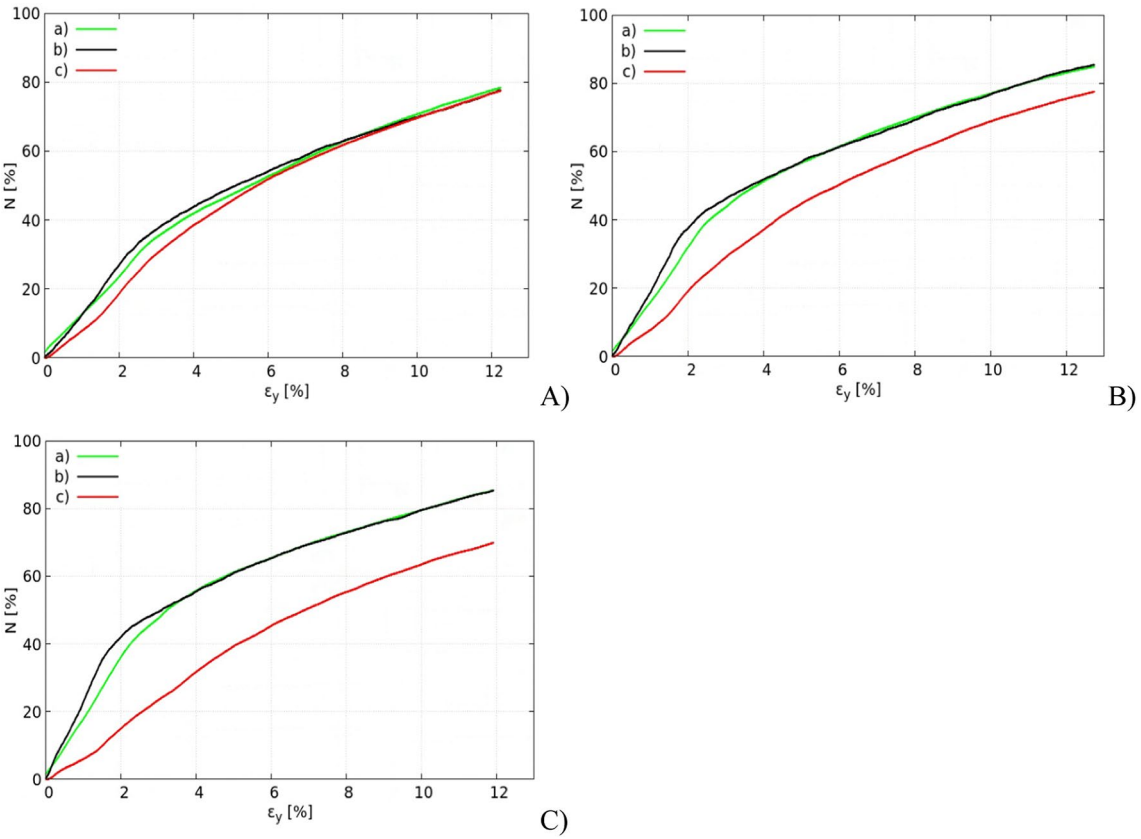

Fig. 13 DEM results with aggregate breakage: relative number of broken contacts N versus vertical normal strain at failure for strain rate $\dot{\epsilon}=1000$ 1/s (mortar parameters multiplied by: **A**) factor 2, **B**) factor 5 and **C**) factor 10): (a) mortar, (b) ITZs and (c) aggregate

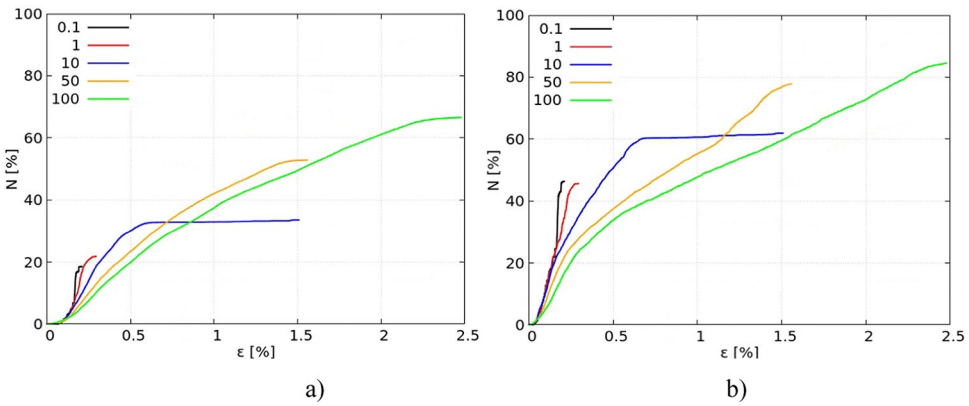

Fig. 14 DEM results with unbreakable and non-deformable aggregate: relative number of broken contacts for different strain rates (0.1 1/s$\leq\dot{\epsilon}\leq$100 1/s): (**a**) mortar and (**b**) ITZs

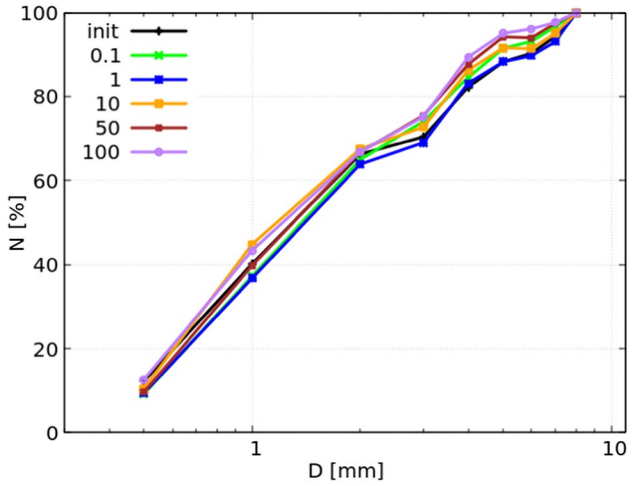

Fig. 15 Relative aggregate number N [%] versus minimum breakable aggregate diameter D for strain rate $\dot{\epsilon}$ between 0.1 1/s and 100 1/s

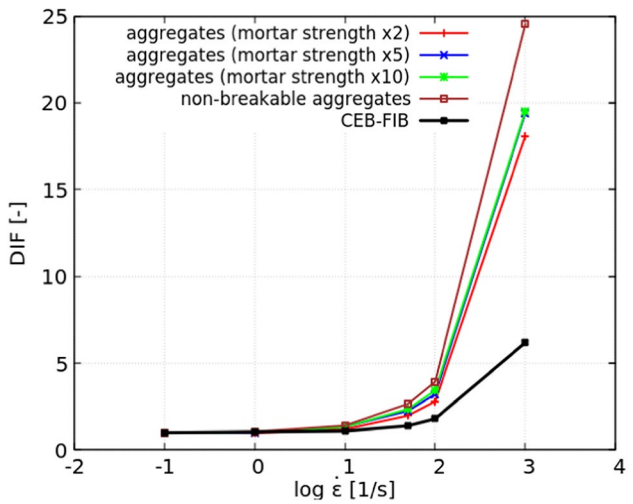

Fig. 16 DEM results: dynamic impact factor DIF during compression against logarithmic strain rate ($\log\dot{\epsilon}$) with various aggregate parameters as compared to CEM-FIP [75]: (**a**) mortar parameters multiplied by factor 2, (**b**) mortar parameters multiplied by factor 5, (**c**) mortar parameters multiplied by factor 10, and (**d**) unbreakable and non-deformable aggregate

Acknowledgements The present study was supported by the research project "*Fracture propagation in rocks during hydro-fracking - experiments and discrete element method coupled with fluid flow and heat transport*" (years 2019–2023), and financed by the National Science Centre (NCN) (UMO-2018/29/B/ST8/00255).

Author contributions M. N.: Investigation, Conceptualization, Methodology, Investigation, Writing – original draft, Writing – review & editing, J.T.: Conceptualization, Methodology, Writing – original draft, Writing – review & editing.

Data availability Data is provided within the manuscript.

Declarations

Conflict of interest The authors declare no competing interests.

References

1. Watstein, D.: Effect of straining rate on the compressive strength and elastic properties of concrete. J Am Concrete Inst **49**(4), 729–744 (1953)
2. Bischoff, P.H., Perry, S.H.: Compressive behaviour of concrete at high strain rates. Mater. Struct. **24**(6), 425–450 (1991)
3. Fu, H.C., Erki, M.A., Seckin, M.: Review of effects of loading rate on concrete in compression. J. Struct. Eng. **117**(12), 3645–3659 (1991)
4. You, J.H., Hawkins, N.M., Kobayashi, A.S.: Strain-rate sensitivity of concrete mechanical properties. ACI Mat J **89**(2), 146–153 (1992)
5. Malvar, L.J., Ross, C.A.: Review of strain rate effects for concrete in tension. ACI Mater. J. **95**, 435–439 (1998)
6. Li, Q., Meng, H.: About the dynamic strength enhancement of concrete-like materials in a split hopkinson pressure bar test. International Journal of Solids and Structures **40**(2), 343–60 (2003)
7. Reinhardt, H.W., Weerheijm, J.: Tensile fracture of concrete at high loading rates taking into account of inertia and crack velocity effects. Int. J. Fracture **51**, 31–42 (1991)
8. Rossi, P.: A physical phenomenon which can explain the mechanical behaviour of concrete under high strain rates. Mater. Struct. **24**(6), 422–424 (1991)
9. Cadoni, E., Labibes, K., Albertini, C.: Strain-rate effect on the tensile behavior of concrete at different relative humidity levels. Mater. Struct. **34**, 21–26 (2001)
10. Rossi, P., Boulay, C.: Influence of free water in concrete on the cracking process. Mag. Concr. Res. **42**, 143–146 (1990)
11. Rossi, P.: Influence of cracking in presence of free water on the mechanical behavior of concrete. Mag. Concr. Res. **43**, 53–57 (1991)
12. Bažant, Z.P., Caner, F.C.: Impact comminution of solids due to local kinetic energy of high shear strain rate: I Continuum theory and turbulence analogy. J Mech Phys Solids **64**, 223–235 (2014)
13. Zhang, X., Chiu, Y.-W., Hao, H., Cui, J.: Free water effect on the dynamic compressive properties of mortar. Cement Concr. Compos. **118**, 103933 (2021)
14. Yu, Q., Zhuang, W., Shi, C.: Research progress on the dynamic compressive properties of ultra-high performance concrete under high strain rates. Cement Concr. Compos. **124**, 104258 (2021)
15. Krzaczek, M., Tejchman, J., Nitka, M.: Effect of free water on the compression behaviour of partially-saturated concrete with a fully coupled DEM/CFD approach. Granular Matter **26**, 38 (2024)
16. Krzaczek, M., Tejchman, J., Nitka, M.: Coupled DEM/CFD analysis of impact of free water on the static and dynamic response of concrete in tension regime. Comput. Geotech. **172**, 106449 (2024)

17. Nitka, M.: Static and dynamic concrete calculations: breakable aggregates in DEM model. Journal of Building Engineering **89**, 109006 (2024)
18. Skarżyński, L., Nitka, M., Tejchman, J.: Modelling of concrete fracture at aggregate level using FEM and DEM based on x-ray μCT images of internal structure. Eng. Fract. Mech. **10**(147), 13–35 (2015)
19. Suchorzewski, J., Tejchman, J., Nitka, M.: Experimental and numerical investigations of concrete behaviour at meso-level during quasi-static splitting tension. Theoret. Appl. Fract. Mech. **96**, 720–739 (2018)
20. Nitka, M., Tejchman, J.: A three-dimensional meso scale approach to concrete fracture based on combined DEM with X-ray μCT images. Cem. Concr. Res. **107**, 11–29 (2018)
21. Zhang, M., Li, Q.M., Huang, Wu., H.J., Lu, Y.B.: Inertia-induced radial confinement in an elastic tubular specimen subjected to axial strain acceleration. Int. J. Impact Eng. **37**(4), 459–464 (2010)
22. Xia, K., Wei, Y.: Dynamic rock tests using split Hopkinson (Kolsky) bar system—a review. Journal of Rock Mechanics and Geotechnical Engineering **7**, 27–59 (2015)
23. Flores-Johnson, E.A., Li, Q.M.: Structural effects on compressive strength enhancement of concrete-like materials in a split Hopkinson pressure bar test. Int. J. Impact Eng **109**, 408–418 (2017)
24. Grote, D.L., Park, S.W., Zhou, M.: Dynamic behavior of concrete at high strain rates and pressures: I. experimental characterization. Int J Impact Eng **25**(9), 869–86 (2001)
25. Huang, R., Guan, Z., Qin, J., Wen, Y., Lai, Z.: Strain rate effect of concrete based on split Hopkinson pressure bar (SHPB) test. Journal of Building Engineering **86**, 108856 (2024)
26. Cao, S., Hou, X., Rong, Q., Zheng, W., Abid, M., Li, G.: Effect of specimen size on static strength and dynamic increase factor of high-strength concrete from SHPB. Constr. Build. Mater. **194**, 71–82 (2019)
27. Wang, S., Zhang, M.-H., Quek, S.T.: Effect of specimen size on static strength and dynamic increase factor of high-strength concrete from SHPB test. J. Test. Eval. **39**, 5 (2011)
28. Li, X.Q., Chen, Q.J., Chen, J.F., Liao, J.Z., Lu, Y.: Dynamic increase factor (DIF) for concrete in compression and tension in FE modelling with a local concrete model. International Journal of Impact Engineering **2022**(163), 104079 (2022)
29. Zhu, X.C., Zhu, H., Li, H., Ran, H.: Drop-Weight Impact Test on U-Shape Concrete Specimens with Statistical and Regression Analyses. Materials **8**(9), 5877–5890 (2015)
30. Zhang, J., Zhang, G., Sun, X., Pan, W., Huang, P., Li, Z., Baoyun Zhang, B., Zhou, X.: Analysis of compressive dynamic behaviors of plain concrete and lightweight aggregate concrete. Case Studies in Construction Materials **15**, e00557 (2021)
31. Chiu, Y.-W., Hao, H., Cui, J., Zhang, X.: Free water effect on the dynamic compressive properties of mortar. Cement Concr. Compos. **118**, 103933 (2021)
32. Fu, Q., Zhang, Z., Zhao, X., Hong, M., Guo, B., Yuan, Q., Niu, D.: Water saturation effect on the dynamic mechanical behaviour and scaling law effect on the dynamic strength of coral aggregate concrete. Cement Concr. Compos. **120**, 104034 (2021)
33. Sun, X., Wang, H., Cheng, X., Sheng, Y.: Effect of pore liquid viscosity on the dynamic compressive properties of concrete. Constr. Build. Mater. **231**, 117143 (2020)
34. Wang, Q., Liu, Y., Peng, G.: Effect of water pressure on mechanical behavior of concrete under dynamic compression state. Constr. Build. Mater. **125**, 501–509 (2016)
35. Li, M., Hao, H., Shi, Y., Hao, Y.: Specimen shape and size effects on the concrete compressive strength. Constr. Build. Mater. **161**(2018), 84–93 (2018)
36. Ahmad, S.H., Shah, P.: Behaviour of hoop confined concrete under high strain rates. ACI J. **82**, 634–647 (1984)
37. Cotsovos, D.M., Pavlovic, M.: Parametric investigation of factors affecting the behaviour of prismatic concrete specimens under high loading rates of uniaxial compressive loading'. Paper Presented at First South-East European Conference on Computational Mechanics, Kragujevac, Serbia and Montenegro 28/06/06–30/06/06 (2006)
38. Bolander, J.E., Eliáš, J., Cusatis, G., Nagai, K.: Discrete mechanical models of concrete fracture. Eng. Fract. Mech. **257**, 108030 (2021)
39. Nitka, M., Tejchman, J.: Modelling of concrete behaviour in uniaxial compression and tension with DEM. Granular Matter **17**(1), 145–164 (2015)
40. Suchorzewski, J., Tejchman, J., Nitka, M.: Discrete element method simulations of fracture in concrete under uniaxial compression based on its real internal structure. Int. J. Damage Mech **27**(4), 578–607 (2014)
41. Suchorzewski, J., Tejchman, J., Nitka, M., Bobinski, J.: Mesoscale analyses of size effect in brittle materials using DEM. Granular Matter **21**(9), 1–19 (2019)
42. Nitka, M., Tejchman, J.: Meso-mechanical modelling of damage in concrete using discrete element method with porous ITZs of defined width around aggregates. Eng. Fract. Mech. **231**, 107029 (2020)
43. Nitka, M., Tejchman, J.: Mesoscopic simulations of a fracture process in reinforced concrete beam in bending using a 2D coupled DEM/micro-CT approach. Eng. Fract. Mech. **2304**, 110153 (2024)
44. Tomporowski, D., Nitka, M., Tejchman, J.: Application of the 3D DEM in the modelling of fractures in pre-flawed marble specimens during uniaxial compression. Eng. Fract. Mech. **277**, 108978 (2023)
45. Lobo-Guerrero, S., Vallejo, L.E.: Discrete element method analysis of railtrack ballast degradation during cyclic loading. Granular Matter **8**(3–4), 195–204 (2006)
46. Lee, H., Kwon, J.H., Kim, K.H., Cho, H.C.: Application of DEM model to breakage and liberation behaviour of recycled aggregates from impact-breakage of concrete waste. Miner. Eng. **21**, 761–765 (2008)
47. Lu, M., McDowell, G.R.: Discrete element modelling of railway ballast under monotonic and cyclic triaxial loading. Geotechnique **60**(6), 459–467 (2010)
48. Indraratna, B., Thakur, P.K., Vinod, J.S.: Experimental and numerical study of railway ballast behavior under cyclic loading. Int. J. Geomech. **10**(4), 136–144 (2010)
49. Xu, M., Hong, J., DEM Song, E.: study on the effect of particle breakage on the macro- and micro-behavior of rockfill sheared along different stress paths. Comput. Geotech. **89**, 113–127 (2027)
50. Fu, R., Hu, X., Zhou, B.: Discrete element modeling of crushable sands considering realistic particle shape effect. Comput. Geotech. **91**, 179–191 (2017)
51. Iliev, P.S., Wittel, F.K., Herrmann, H.J.: Evolution of fragment size distributions from crushing of granular materials. Phys. Rev. E **99**, 012904 (2019)
52. Zhang, T., Zhang, C., Zou, J., Wang, B., Song, F., DEM Weihao, Y.: exploration of the effect of particle shape on particle breakage in granular assemblies. Comput. Geotech. **122**, 103542 (2020)
53. Harmoa, J.M., Arthur, D., Andrade, J.E.: Level set splitting in DEM for modeling breakage mechanics. Comput. Methods Appl. Mech. Engrg. **365**, 112961 (2020)
54. Alabbasi, Y., Hussein, M.: Geomechanical modelling of railroad ballast: a review. Arch Comput Methods Eng **28**(3), 815–839 (2021)
55. Brzezinski, K., Gladky, A.: Clump breakage algorithm for DEM simulation of crushable aggregates. Tribol. Int. **173**, 107661 (2022)

56. Foldager, F.F., Munkholm, L.J., Balling, O., Serban, R., Negrut, D., Heck, R.J., Green, O.: Modeling soil aggregate fracture using the discrete element method. Soil & Tillage Research **218**, 105295 (2022)
57. Zhang, C., Chen, Y., Wang, Y., Bai, Q.: Discrete element method simulation of granular materials considering particle breakage in geotechnical and mining engineering: a short review. Green and Smart Mining Engineering **1**, 190–207 (2024)
58. Liu, M., Wang, F.: Numerical simulation of influence of coarse aggregate crushing on mechanical properties of concrete under uniaxial compression. Constr. Build. Mater. **342**, 128081 (2022)
59. Kozicki, J., Donze, F.V.: A new open-source software developer for numerical simulations using discrete modeling methods. Comput. Methods Appl. Mech. Eng. **2197**, 4429–4443 (2008)
60. Šmilauer, V. et al.: Yade Documentation 3rd ed. The Yade Project. 10.5281/zenodo.5705394 http://yade-dem.org/doc/, 2021.
61. Cundall, P., Strack, O.: A discrete numerical model for granular assemblies. Géotechnique **29**(1), 47–65 (1979)
62. Cundall, P., Hart, R.: Numerical modelling of discontinua. Eng. Comput. **9**, 101–113 (1992)
63. Leśniewska, D., Nitka, M., Tejchman, J., Pietrzak, M.: Contact force network evolution in active earth pressure state of granular materials: photo-elastic tests and DEM. Granular Matter **22**(3), 71 (2020)
64. Kozicki, J., Niedostatkiewicz, M., Tejchman, J., Mühlhaus, H.-B.: Discrete modelling results of a direct shear test for granular materials versus FE results. Granular Matter **15**(5), 607–627 (2013)
65. Kozicki, J., Tejchman, J., Műhlhaus, H.-B.: Discrete simulations of a triaxial compression test for sand by DEM. Int. J. Num. Anal. Meth. Geomech. **38**, 1923–1952 (2014)
66. Kozicki, J., Tejchman, J.: Relationship between vortex structures and shear localization in 3D granular specimens based on combined DEM and Helmholtz-Hodge decomposition. Granular Matter **20**, 48 (2018)
67. Krzaczek, M., Kozicki, J., Nitka, M., Tejchman, J.: Simulations of hydro-fracking in rock mass at meso-scale using fully coupled DEM/CFD approach. Acta Geotech. **15**, 297–324 (2020)
68. Krzaczek, M., Nitka, M., Tejchman, J.: Effect of gas content in macropores on hydraulic fracturing in rocks using a fully coupled DEM/CFD approach. Int. J. Numer. Anal. Meth. Geomech. **45**(2), 234–264 (2021)
69. Tejchman, J., Bobinski, J.: Continuous and discountinous modelling of fracture in concrete using FEM. Springer, Berlin (2013)
70. Skarżyński, L., Tejchman, J.: Experimental investigations of fracture process in concrete by means of x-ray micro-computed tomography. Strain **52**, 26–45 (2026)
71. Xiao, J., Li, W., Suc, Z., Lange, D.A., Shah, S.P.: Properties of interfacial transition zones in recycled aggregate concrete testes by nanoindentation. Cement Concr. Compos. **37**, 276–292 (2013)
72. Kozicki, J., Tejchman, J., Mróz, Z.: Effect of grain roughness on strength, volume changes, elastic and dissipated energies during quasi-static homogeneous triaxial compression using DEM. Granular Matter **14**, 457–468 (2012)
73. Xi, Y., Wenhua, Z., Yilin, P., Wanting, Z., Fenghao, Y.: Comparative study on damping test methods of concrete materials. Constr. Build. Mater. **300**, 124367 (2021)
74. Ng, T.-T., Zhou, W., Ma, G., Chang, X.-L.: Damping and Particle Mass in DEM Simulations under Gravity. J. Eng. Mech. **141**(6), 04014167 (2014)
75. Fib Model Code for concrete structures. Lausanne: international Federation for Structural Concrete (2013)
76. Krzaczek, M., Tejchman, J., Nitka, M.: The static/dynamic response of partially saturated concrete using an improved fully coupled DEM/CFD approach. In: ASCE Engineering Mechanics Institute 2024 International Conference, 11–13.09.2024, Vienna, Austria (2024)